Aerodynamic Influence Coefficient Computations Using Euler/Navier-Stokes Equations On Parallel Computers

Chansup Byun (MCAT Inc.)*, Mehrdad Farhangnia (MCAT Inc.)†
Guru P. Guruswamy (NASA)‡
Aeronautical Information Technology Division
NASA Ames Research Center, Moffett Field, California 94035-1000

Abstract

An efficient procedure to compute aerodynamic influence coefficients (AIC) using high fidelity flow equations such as Euler/Navier-Stokes equations is presented. The AIC's are computed by perturbing structures using mode shapes. The procedure is developed on a multiple-instruction, multiple-data (MIMD) parallel computer. In addition to discipline parallelization and coarse-grain parallelization of the flow domain, embarrassingly parallel implementation of ENSAERO code demonstrates linear speedup for a large number of processors. Demonstration of the AIC computation for static aeroelasticity analysis is made on an arrow wing-body configuration. Validation of the current procedure is made on a straight wing with arc-airfoil at a subsonic region. The present flutter speed and frequency of the wing show excellent agreement with those results obtained by experiment and NASTRAN. The demonstrated linear scalability for multiple concurrent analyses shows that the three-level parallelism in the code is well suited for the computation of the AIC's.

Introduction

Modern design requirements for aircraft push current technologies used in the design process to their limits or sometimes require more advanced technologies to meet the requirements. One of the many essential things needed to improve the performance is accurate prediction of aerodynamic loads. In the current design process, the linear aerodynamics are widely used to predict aerodynamic loads. However, the linear aerodynamics may not be adequate for the design of an advanced subsonic civil transport. Since the fluid flow shows strong nonlinearities at the transonic regime, high fidelity equations, such as the Euler or Navier-Stokes equations, can predict flow characteristics more accurately than the linear aerodynamics.

However, high fidelity flow equations are computationally expensive and require an order of magnitude longer time to obtain aerodynamic loads required in the design. The costs become particularly acute in flutter analyses since there are a large number of analysis conditions. Since traditional aeroelastic analysis has been performed with quite a modest amount of computer time, it has been difficult to justify using high fidelity flow equations in a preliminary design environment.[1] Parallel computing is one possibility to cut down the computational turnaround time in using high fidelity equations so that high fidelity equations could be incorporated into the preliminary design process.

The present investigation uses the ENSAERO code, which is capable of computing aeroelastic responses by simultaneously integrating the Euler/Navier-Stokes equations and the modal or the finite element structural equations of motion using aeroelastically adaptive dynamic grids.[2-6] The patched zonal grid technology based on the work in Ref. 7 has been implemented for the flow computations of rigid complex geometries. The code has been applied to transonic flows over fighter wings undergoing unsteady motions at small to moderately large angles of attack.[3-5] The code has been extended to simulate unsteady flows over rigid wing and wing-body configurations with an oscillating trailing edge flap by using either single or patched multizonal grids.[5-6] The code has been parallelized and used for aeroelastic computations for wing and wing-body configurations[8] on the Intel iPSC/860 parallel computer, using a single zone computational grid for the fluids.

Furthermore, the numerical simulation of flows over complex geometries typically requires the use

---

*Senior Research Scientist, AIAA Member, currently employed by Sun Microsystems Inc.
†Research Scientist, AIAA Member
‡Senior Research Scientist, AIAA Associate Fellow

of a multizonal method. This method is based on domain decomposition techniques, with the flow domain being partitioned into a number of subdomains (zones). Within each subdomain, the flow equations are solved in an independent manner, with the global nature of the flow being accounted for by the periodic exchange of boundary information between neighboring zones. Thus, the multizonal method for fluids has been integrated into the aeroelasticity analysis process to simulate problems involving flexible complex geometries.[9] The code has been parallelized based on the multizonal method on the IBM SP2 parallel computer, which is a MIMD type parallel computer.[9] This type of parallelization is called "coarse grain" parallelization in contrast to "fine grain" parallelization which parallelizes a solver itself without introducing explicit zonal boundaries. A demonstration computation for static aeroelasticity simulation has been made for an arrow wing-body configuration[9,10] using the parallel version of ENSAERO.

Since this parallel implementation is based on the multizonal method, there may be significant load imbalance between processors. This load imbalance can be avoided by designing the size of each grid block to be as close to each other as possible. Load balancing can also be achieved by decomposing each grid block into smaller sub-grids in conjunction with the fine grain parallelization of the flow solver. However, this is not considered here since it is beyond the scope of this paper.

This paper presents an efficient procedure on MIMD parallel computers to obtain the AIC's based on mode shapes by solving the Euler/Navier-Stokes equations. Demonstration computations are performed for an arrow wing-body configuration, which has been studied as a design concept for supersonic civil transport.[11] This model is selected for validation of steady flow computations since experimental data for surface pressure distributions are well documented. In addition, as a validation of the current procedure, the present flutter speed and frequency of a straight wing with 6% thick arc-airfoil is compared with those results obtained by the experiment[26] and NASTRAN. The results show excellent agreement with each other. Since the procedure uses a high fidelity flow solver with multizonal capability, it can be used to compute the AIC's for more complex configurations in the transonic regime.

AIC's in Aeroelasticity Analysis

The governing aeroelastic equations of motion can be formulated by using the Rayleigh-Ritz method. In this method, the resulting aeroelastic displacements at any time are expressed as a function of a finite set of assumed modes. The contribution of each assumed mode to the total motion is derived by Lagrange's equation. Furthermore, it is assumed that the deformation of the structure can be represented by deflections at a set of discrete points. From this assumption, the displacement vector $\{d\}$ can be expressed as

$$\{d\} = [\Phi]\{h\} \tag{1}$$

where $[\Phi]$ is the modal matrix and $\{h\}$ is the generalized displacement vector.

The final matrix form of the aeroelastic equations of motion is

$$[M]\{\ddot{h}\} + [G]\{\dot{h}\} + [K]\{h\} = \{Z\} \tag{2}$$

where $[M]$, $[G]$, and $[K]$ are the modal mass, damping, and stiffness matrices, respectively. The vector $\{Z\}$ is the modal aerodynamic force vector.

With the above modal equations of motion, the flutter boundary can be computed by using coupled and uncoupled approaches.[12] The coupled approach requires direct time integration of flow and structural equations. Although this approach is accurate for flows with strong nonlinearities, it is computationally expensive. On the other hand, the uncoupled approach which is computationally less expensive, requires an additional assumption that the aerodynamic data can be linearly superimposed among the vibration modes. As demonstrated in Refs. 12 and 13, and more recently in Ref. 14, the uncoupled method can be an effective approach to predict the preliminary flutter characteristics required in early stages of design. Based on the flutter computations of airfoils in Ref. 12, the uncoupled approach requires one-tenth of the computational effort required for the coupled analysis. In this work, the traditional U-g method, which is the uncoupled approach, is selected to demonstrate the application of the AIC's in the aeroelasticity analysis procedure. The U-g method assumes that the structure will be undergoing simple harmonic motion so that the generalized coordinates $\{h\}$ take the form

$$\{h\} = \{\bar{h}\}e^{i\omega t} \tag{3}$$

where ω is the frequency of oscillation at flutter. Since the modal aerodynamic force vector is obtained by perturbing the structure, it is assumed as

$$\begin{aligned} \{Z\} &= [\Phi]^T(\tfrac{1}{2}\rho U^2 c[S]\{d\}) \\ &= \tfrac{1}{2}\rho U^2 c[\Phi]^T[S][\Phi]\{h\} \\ &= \tfrac{1}{2}\rho U^2 c[Q]\{h\} \end{aligned} \tag{4}$$

where ρ is the free-stream flow density, U is the free-stream flight speed, c is the reference chord length.

[S] is the diagonal force matrix and is obtained by integrating pressure over the structure surface. $[\Phi]$ is the modal matrix. $[Q]$ is the generalized aerodynamic force matrix on the modal coordinates system. Thus the generalized aerodynamic force Q_{ij} can be written as

$$Q_{ij} = \{\phi_i\}^T[S]\{\phi_j\} \tag{5}$$

The coefficient Q_{ij} represents the force acting in the i^{th} mode due to pressure generated by the modal motion associated with the j^{th} mode. The force matrix $[S]$ can be computed by using the AIC's defined below.

The aerodynamic influence coefficients based on modal modes are defined as the following equation.

$$\Delta C_{Pj} = [A]\{\phi_j\} \tag{6}$$

where ΔC_{Pj} is the change of the pressure coefficients induced by the modal deformation on the j^{th} mode shape and $\{\phi_j\}$ is the j^{th} mode shape. The aerodynamic influence coefficient denotes the change of the pressure at i^{th} surface point due to the unit modal deformation of the j^{th} mode shape. The AIC matrix is defined as(Ref. 15)

$$[A] = [\Delta C_P]([\Phi]^T[\Phi])^{-1}[\Phi]^T \tag{7}$$

where $[\Phi]$ is the modal matrix composed of the vibration modes and $[\Delta C_P]$ is the matrix composed of the vector, ΔC_{Pj}. By solving the Euler or Navier-Stokes flow equations with forced structural motion based on a selected mode shape, ENSAERO can compute the AIC matrix in concurrent fashion. Then the AIC's can be used to obtain the aerodynamic forces by using Eq. (6) when the structure has changed.

Substituting Eqs. (3) and (4) into Eq. (2) and introducing the concept of artificial damping,[16] Eq. (2) can be represented as a set of complex eigenvalue equations given by

$$\begin{gathered} [K]^{-1}[[M] + C[Q]]\{\bar{h}\} = \lambda\{\bar{h}\} \\ C = \frac{\rho c^3}{2k^2} \\ \lambda = \frac{(1+ig)}{\omega^2}, \text{ complex eigenvalue} \\ k = \frac{\omega c}{U}, \text{ reduced frequency} \end{gathered} \tag{8}$$

where g is the artificial damping coefficient. Since the coefficient Q_{ij} is computed from the unsteady motion, it is dependent on the reduced frequency which is implicitly included in ΔC_p. For each reduced frequency chosen, the generalized aerodynamic force matrix $[Q]$ is obtained by solving the unsteady flow equations and then, in turn, the complex eigenvalue problem, Eq. (8), can be solved to obtain the damping coefficient, g. There are several approaches[12,14,17–19] to compute the generalized aerodynamic force matrix. Byun and Guruswamy[20] compared the time integration and pulse transfer-function approaches to compute the generalized aerodynamic force matrix for a wing configuration. In this work pulse transfer-function approach is used for computing AIC.

For divergence prediction, by dropping out all time-dependent terms in Eq. (2) the resulting equations can be given by

$$[K]\{\bar{h}\} = q_{div}c[Q]\{\bar{h}\} \tag{9}$$

where q_{div} is the divergence dynamic pressure for a given flight condition. For static aeroelasticity analysis, the aerodynamic influence coefficient matrix is obtained from a steady flow solution of a perturbed configuration associated with a particular mode shape selected as an input. The perturbation amplitude of the structure depends on the flow characteristics and the moving grid capability. The perturbation from a steady solution should be small enough so that a linear superposition of the solution is applicable to the response. The perturbation is incrementally applied to deform the structure until it reaches a given perturbation amplitude. In order to obtain converged flow solutions at a perturbed state, additional number of iterations for the flow solution is performed while fixing the deformed fluid grid at the final state.

Parallel Implementation

The domain decomposition approach used in ENSAERO is suitable for parallelization. The discipline parallelization is achieved by distributing the fluid, structure and control domains onto different groups of processors. Only a single processor is assigned to the structure and control groups since the respective computational loads are relatively small. The fluid domain is further parallelized based on the multizonal method. This method partitions the fluid domain into several subdomains (zones) and solves the flow equations of each zone independently. Therefore, parallelization of the fluid domain is achieved by assigning one processor to each of the zones in the fluid domain. Each processor solves the flow equations of each zone concurrently. Then, the zonal boundaries are updated by exchanging boundary information between neighboring zones.

The data communication between different discipline modules and between fluid zones is accomplished by using the Message Passing Interface (MPI)[21] standard, which is a set of library interface standards for message passing. The partitioning of processors, loading and execution of different programs onto processors are enabled by using the

MPIRUN[22] library, which is a utility developed by the NAS Parallel Systems Group at NASA Ames Research Center. MPIRUN flexibly allocates a group of processors and enables point-to-point communication within a group or between groups. MPIRUN is based on the MPI standard, thus the parallel version of ENSAERO should run without modification on any MIMD-type computer supporting the MPI standard. For demonstration purposes, the IBM SP2 computer is selected.

The serial version of ENSAERO treats each zone of the domain sequentially, while the other zones reside in a secondary storage device such as the SSD on a Cray C90. The main difference between the serial and parallel version is that the parallel implementation exploits the functional parallelism among multiple zones of patched grids. As a result, all zones are computed concurrently.

The interpolation and communication of the zonal boundary data is also done concurrently, through a loosely synchronous approach. At the end of each time step, processors holding zonal boundary surfaces send the interpolated flow field data to the appropriate processors of the other zones. Each processor proceeds to the computations of the next time step of the flow solver as soon as its zonal communication phase is completed.

In order to couple the fluid, structure and control domains, communication between domains is also accomplished through an interface at the end of each time step. The aerodynamic loads are converted into the structural loads through the fluid-structural interface.[8,23] Furthermore, the structural deformation is passed to the fluid domain through the interface. Then, the surface grid is deformed according to the structural deformation. In addition, control surface deflection is superimposed on the deformed surface grid.

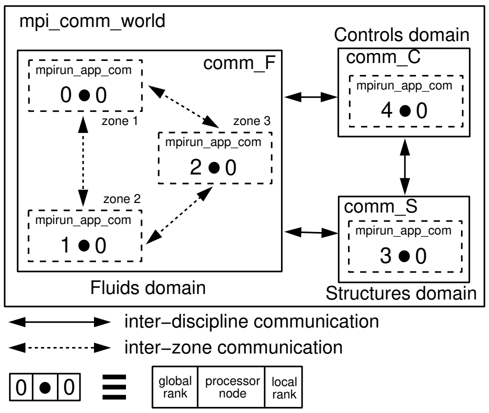

Fig. 1. Data communication design in a multizonal ENSAERO code on MIMD parallel computers.

The overall communication design is shown in Fig. 1. In using the MPI library, a communicator is used to identify a group of processors so that a processor can communicate with others within the same group. Each group is represented by a box defined by dashed lines as shown in Fig. 1. In this case, however, only one processor is assigned to each group for a single coupled analysis. All the allocated processors have a common communicator called mpi_comm_world as shown in Fig. 1. The MPIRUN utility creates a distinct communicator, denoted as mpirun_app_com in Fig. 1, for each group of computational nodes when it loads the executable program onto the processors. Using the mpirun_app_com communicator, any processor can communicate with others within a group. In order to communicate between different discipline modules or different groups, communicators for inter-discipline and inter-zone communications are also defined using the MPIRUN library. They are denoted by solid and dashed lines with arrows, respectively.

Furthermore, the MPI library has the functionality to create a new communicator for a subset of the allocated processors. Communicators for each discipline are defined so that collective operations can be accomplished within a discipline module. Once a communicator for each discipline is defined, it is quite convenient to do a collective operation within a discipline, such as computing lift and drag coefficients. The communication design shown in Fig. 1 only explains the coupling of three different computational modules, e.g. fluids, structures, and controls. However, if needed, additional module can be easily added to the existing modules.

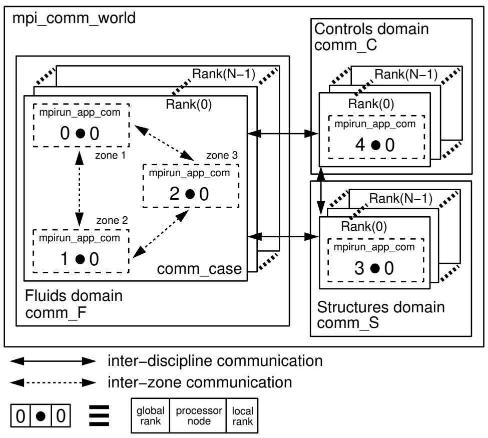

Fig. 2. Data communication design suitable for multiple coupled analyses in a multizonal ENSAERO code on MIMD parallel computers.

The communication design for a single coupled analysis can be further extended to perform multiple analyses concurrently. Figure 2 shows the extension of the communication design for concurrent multiple analyses. As contrast to a single coupled analysis, several processors are assigned to each group. In this figure, each group has N processors, which is the number of different cases running concurrently. They are locally ranked from zero to N-1 within a group. In the first run, the initialization data within a group is distributed from the leading node of each group through a broadcast call using mpirun_app_com communicator. This makes it easy to distribute initial input data within a group. Once the initial data distribution is completed, each processor of a group will participate in a different analysis. For example, if N cases with different initial angles of attack are concurrently executed, each processor within a group has the same grid data of a zone but computes solutions for the different flow condition, which in this case is a different angle of attack. Within the flow domain, after solving the flow equations at every time step, each zone needs to exchange zonal boundary data with adjacent zones to advance to the next step. For this purpose, data communication is limited only among computational nodes with the same local rank. In this communication strategy, each node can distinguish itself from other nodes assigned to different cases. Therefore, each node having different local rank can participate in different simulations. For multiple multidisciplinary simulations, the same communication strategy is applied for data exchange among the discipline domains.

Figure 3 shows the scalability and performance of the parallel version of ENSAERO. To obtain a performance measurement on the code, a scalability and performance study is done using a wing-body-empennage configuration. This configuration consists of a single block H-O grid with 180x173x40 points in the streamwise, spanwise, and body-normal directions, respectively. The grid is split into multiple, equally sized zones cut perpendicular to the streamwise direction, with each zone assigned to a separate processor. Timing functions are utilized to exclude initialization and I/O CPU usage, thus only the solver portion of the code is represented.

Figure 3(a) shows the scalability of the code for steady fluids computations. The solid line represents the ideal linear speedup. Two levels of parallelism are shown in this figure. The single parameter set shows continued splitting of the volume grid from 9 to 36 zones. The multiple parameter set represents executing multiple 9 zone cases concurrently with various angles of attack.

For both single and multiple parameter cases, using this coarse grain parallelism, the code scales up nicely with the increase in the number of processors. The rate of scalability of this type of coarse grain parallelism is encouraging. With efforts in progress to include the functionality of fine grain parallelism, which has already been implemented and demonstrated,[8] the computational potential of parallel machines will be more fully utilized by this code.

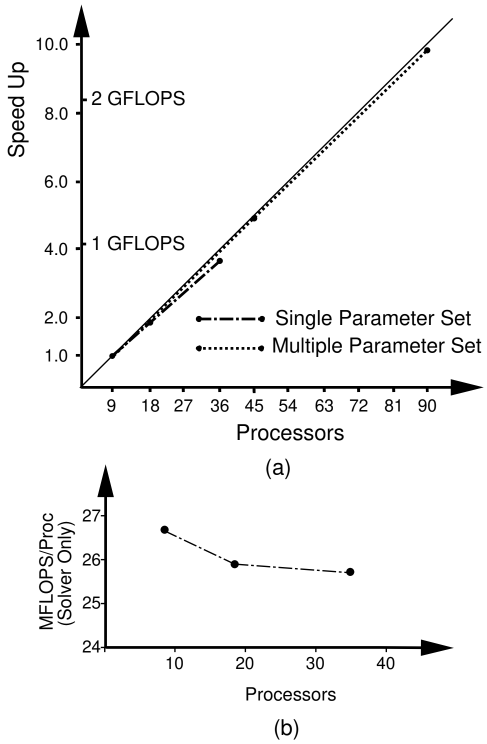

Fig. 3. Scalability and performance of ENSAERO on the SP2 parallel computer.

The CPU speed of the flow solver is shown in Fig. 3(b) in MFLOPS/processor. This shows that the performance is decreased as the number of grid blocks is increased for a single analysis case. This is mainly due to increase in the ratio of communication and computation time per node. The code ran consistently near 26 MFLOPS/processor, which corresponds approximately 100 μs/grid pt/step for a single node case on SP2 that composed of RS6000/590 work stations(POWER-2 multi chip with 66.7 MHz clock rate). Another way to measure it is to say that if ENSAERO utilized the full 140 processors on the IBM SP2, one can expect over 3.6 GFLOPS performance.

Model Geometry and Grid

Figure 4 shows the geometry of the wind tunnel model. This model is used for demonstration of

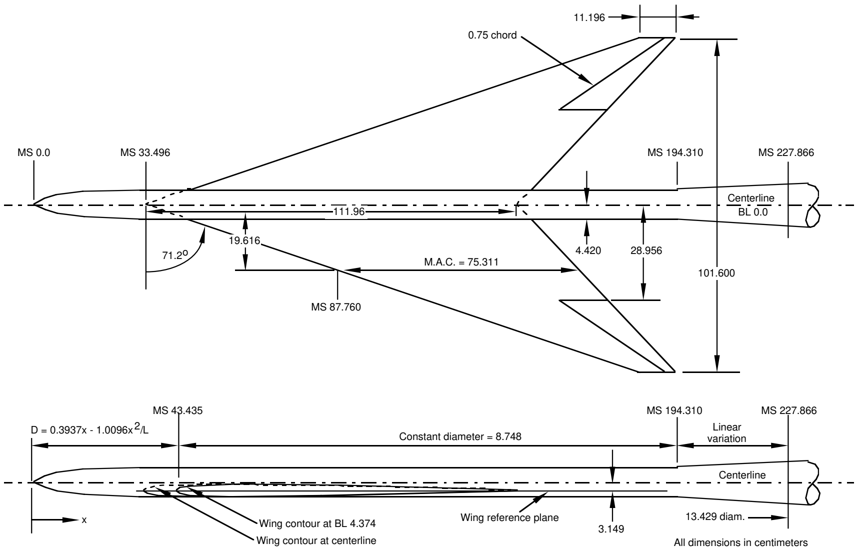

Fig. 4. Wind-tunnel model geometry of an arrow wing-body configuration.

the AIC computations in this study. The configuration has a thin, low aspect ratio, highly swept wing mounted below the centerline of a slender body. The wing is flat with a rounded leading edge. It should be noted that the exact wing tip definition was not available so the tip thickness was decreased to zero across three grid points.

An H-H topology grid is used for the wing-body configuration with a trailing edge flap control surface. This grid topology is chosen in order to easily align grid lines with the control surface. The ICEM-CFD software system[24] is used to generate the surface grid. From the surface grid, the volume grid is generated by using the HYPGEN code.[25] Although the experimental model[11] has two flaps at both the leading edge and the trailing edge, only the outboard flap at the trailing edge is considered in this study.

For the above wing-body configuration detailed validation with the wind tunnel experimental data including grid refinement studies were done and they are reported in detail in Ref. 6. Based the work done in Ref 6, the final grid is selected for this paper. Figure 5 shows an overview of the surface grid for the full-span configuration (every other grid line is shown on the wing). The reference length is the mean aerodynamic chord and the origin of the coordinates is set at the nose of the body. The body extends to the downstream boundary. The half-span grid used for symmetric cases consists of 110 points in the streamwise direction, 116 points in the spanwise direction, and 40 points normal to the body surface, for a total of 510,400 points. Bilateral symmetry is imposed in the x-z plane at y=0 (the center of body). The grid is further divided into upper and lower grids at the wing with the H-topology cut condition at a zonal interface. For the multizonal aeroelastic computations, the original grid was split into 8 patched zonal grids as shown in Fig. 5. Each grid has the same number of grid points and is assigned to one processor on the SP2 computer. Flow variables at the zonal interfaces were updated as soon as the adjoining zones were computed.

Results

Rigid Wing Computations

Figure 6 shows the steady pressures compared with the experiment at 0% (body center), 20%, 50% and 80% semi-spanwise sections for the half-span configuration. The 80% section is located at the mid-span of the control surface. The flow conditions consist of a Mach number of $M_\infty = 0.85$, an angle of attack of $\alpha = 7.93$ degrees, a flap deflection of $\delta = 0$ degree and a Reynolds number of $Re_{\bar{c}} = 9.5 \times 10^6$, based on the mean aerodynamic chord. Baldwin-Lomax turbulence model was used. For the grid selected the y+ value is 3.0. Converged steady state solution was obtained with 2000 time steps during which the residual dropped by three orders of magnitude. Suction observed near the trailing edge at the 80% section corresponds to the leading-edge vortex. There is a discrepancy between the computation and the experiment due to the difference in the location of the leading-edge vortex. The computation predicts the vortex at a slightly more inboard location than the experiment.[6] Possible sources of this difference are the effects of the transition strip and the wall effects of the wind tunnel. No wall cor-

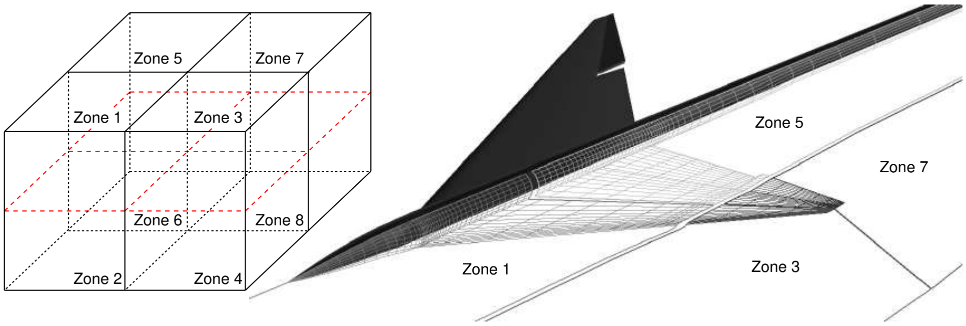

Fig. 5. Overview of the upper surface grid with a deformed control surface and the grid partition for 8 zones.

rections were applied to either the computed or measured data. Overall, the computed results show good agreement with the experiment. The pressure distributions on the body center also show good agreement, as shown in Fig. 6.

Aerodynamic Influence Coefficients

Demonstration of the AIC computation is performed by using the arrow wing-body configuration with the flow conditions used in the rigid computations. The first two vibration modes are used to perturb the structure. In this work, demonstration computations are limited to the AIC's for static aeroelasticity (divergence) analysis.

In the coupled fluid-structure analysis for static aeroelasticity, all the selected vibration modes are used to represent the structural deformation under coupled aerodynamic loads. However, for the AIC computations, only a single mode is selected to perturb the structure. Then, flow solutions are obtained to determine the AIC's due to a particular structural perturbation.

Figure 7 shows the cross-sectional view of deformed wings at two different span stations. Three different perturbation amplitudes of the second vibration mode are enforced to deform the wing. Since the second mode is a twist dominant mode, the local angle of attack changes significantly by changing the perturbation amplitude. As amplitude increases beyond $h_2 = 0.1$, the volume grid used for the flow analysis fails due to the magnitude of the surface grid deformation in this particular simulation. This is mainly due to limitation of the grid shearing scheme to deform the volume grid following the surface deformation. This failure can be avoided by more sophisticated schemes for moving the grid. For $h_2 = 0.1$ case, the vertical difference between the leading and trailing edge points at the wing tip deflection is increased up to 9% of the mean aerodynamic chord length.

The pressure distributions at two span stations, given in Fig. 8, are obtained when the wing is perturbed by two modes with three different amplitudes. The second mode causes significant changes in pressure distribution while the first mode barely changes the pressure distribution at the given span stations as the perturbation amplitudes are increased. As shown in Fig. 7, since the second mode changes local angles of attack significantly, the change in pressure distribution is expected. However, the first mode does not cause any noticeable change in the pressure distribution because it is a bending dominant mode.

Figure 9 shows the total lift and pitching moment coefficients variation with respect to the perturbation amplitudes. The response of the total lift and pitching moment coefficients varies linearly with increasing perturbation amplitude except at the lower perturbation range. A similar trend is obtained on the response of the modal aerodynamic forces for the first and second mode perturbations as shown in Figs. 10 and 11, respectively. Only the first three terms of the modal aerodynamic force vector are presented in the figures.

Using the modal perturbation, the integrated AIC's are obtained for the first and second vibration modes. Just like steady state computations, the convergence criteria is based on the residual. About 9000 time steps were required for residual to drop by about three orders of magnitude. The results are given in Figs. 12 and 13, respectively. As shown in both figures, the A_{11} term, force acting on the first mode due to the first mode perturbation, converges rather slowly compared to the other terms. Overall, at the lower perturbation range, some of the AIC's show that the perturbation amplitude is not large enough to prevail over the existing aerodynamic force by the initial flow condition. However, as perturbation amplitude increases, the AIC's are all converged. Furthermore, it should be noted that the perturbation of the structure should be limited to be in the range of linear superposition of the solution. Otherwise, the response starts to show nonlinear effects, even though the present results were not able to capture these effects because of the grid failure in the flow computation.

Validation

Validation for flutter analysis using the present procedure has been done for a straight rectangular wing with 6% thick parabolic arc airfoil section.[26] The wing has chord and half-span lengths of 4.56 and 11.5 inches, respectively. The structural model is done by using QUAD4 elements available in NASTRAN. The mode shapes are generated by using NASTRAN. The freestream flow conditions are a Mach number of 0.715 and an angle of attack of zero degree. The Euler equations are used in the flow analysis by using ENSAERO with 120,000 grid points while a linear aerodynamics (Doublet-Lattice) method is used in NASTRAN. Two modes, first bending and first torsional, were used to compute AIC values. It required about 1000 time steps for residual to drop by three orders of maginitude during which the response reached a steady state value. Both NASTRAN and ENSAERO results are compared with the experiment as shown in Fig. 14. Solid lines, open and filled symbols represent the results obtained by ENSAERO, NASTRAN and experiment, respectively. The flutter speed and frequency are noted as V_F and ω. Superscripts a, b and E represent NASTRAN, ENSAERO and experiment, respectively. The flutter speeds computed by ENSAERO and NASTRAN are 363 and 339 ft/sec whereas the experimental result is 363 ft/sec. Excellent agreement is obtained between the flutter speeds obtained by experiment and ENSAERO. Also, the flutter frequencies obtained by ENSAERO, NASTRAN, and experiment are 38, 42, and 35 Hz, respectively. ENSAERO predicts the flutter frequency very close to the experimental result as well.

Concluding Remarks

A three level parallel procedure is developed and implemented into a parallel multizonal version of aeroelastic code ENSAERO for the AIC computations. At the first level, parallelization of individual disciplines is done using varying number of processors. In the second level, parallelization is done at the discipline level by running each discipline on a different group of processors. At the third level, multiple aeroelastic cases are run in parallel by dividing the SP2 nodes into different sets of groups. Loading executables onto the SP2 nodes and communicating data between disciplines and between zones is enabled by MPIRUN.[22]

The integrated AIC's are obtained by using the perturbation of the structure based on natural mode shapes. The various results show that the response of the aerodynamic forces is linear for most of the perturbation amplitudes used in this study. However, in this particular case, some of the AIC's do not converge at the lower perturbation range since the perturbation is too small to prevail over the initial aerodynamic forces. As amplitude is increased, the effect of the initial condition disappears. Although the demonstration is only made for static aeroelasticity analysis, this procedure can also be applied to a dynamic aeroelastic problem such as flutter analysis.

The demonstrated linear scalability for the multiple concurrent analyses shows that the three levels of parallelism in the code is well suited for the computation of the AIC's. The code ran consistently near 26 MFLOPS/processor for steady Navier-Stokes fluid computations, which corresponds approximately 100 μs/grid pt/step for a single node case. By using the full 140 processors on the IBM SP2, 3.6 GFLOPS performance is expected for steady Navier-Stokes fluid computations.

This study is on-going work toward aeroelasticity analysis of complete aircraft by using the AIC's based on mode shapes, which are computed by solving high fidelity equations such as the Euler or Navier-Stokes equations on parallel computers. Further study should be made to find the benefit of using high fidelity equations compared to the low fidelity methods using the linear aerodynamics. The current validation work of the code shows excellent agreement between the result obtained by ENSAERO and those results obtained by the experiment and NASTRAN. However, more work is in progress to demonstrate the accuracy of the current method for complex configurations.

Acknowledgments

This work was completed using the resources of the High Performance Computing and Communication Program (HPCCP) and Numerical Aerodynamic Simulation (NAS) Program at NASA Ames Research Center. The work done by the first two authors were funded through NASA Ames Research Center Fluid Dynamics Analysis Contract NAS2-14109. The authors would like to thank Dr. Kumar Bhatia of Boeing Commercial Airplane for his valuable suggestions during this study.

References

[1] Bhatia, K. G. and Wertheimer, J., "Aeroelastic Challenges for a High Speed Civil Transport," AIAA Paper 93-1478-CP, 34th Structures, Structural Dynamics, and Materials Conference, La Jolla, CA, April, 1993, pp. 3661–3682.

[2] Guruswamy, G. P., "Navier-Stokes Computations on Swept-Tapered Wings, Including Flexibility, AIAA Paper 90-1152, April 1990.

[3] Obayashi, S., Guruswamy, G. P. and Goorjian, P. M., "Streamwise Upwind Algorithm for Computing Unsteady Transonic Flows Past Oscillating Wings," AIAA Journal, Vol. 29, No. 10, Oct. 1991, pp. 1668–1667. Errata: AIAA Journal, Vol. 30, No. 2, Feb. 1992, pp. 569.

[4] Obayashi, S. and Guruswamy, G. P., "Unsteady Shock-Vortex Interaction on a Flexible Delta Wing," Journal of Aircraft, Vol. 29, No. 5, Sept.-Oct. 1992, pp. 790–798.

[5] Obayashi, S. and Guruswamy, G. P., "Navier-Stokes Computations for Oscillating Control Surfaces," AIAA Paper 92-4431, August 1992.

[6] Obayashi, S. Chiu, I. and Guruswamy, G. P., "Navier-Stokes Computations on Full-Span Wing-Body Configuration with Oscillating Control Surfaces," AIAA Paper 93-3687, August 1993.

[7] Flores, J., "Simulation of transonic viscous wing and wing-fuselage flows using zonal methods," NASA TM-89421, 1987.

[8] Byun, C. and Guruswamy, G. P., "Wing-Body Aeroelasticity on Parallel Computers," AIAA Journal, Vol. 33, No. 2, Mar.-Apr. 1996, pp. 421–428.

[9] Byun, C. and Guruswamy, G. P., "Aeroelastic Computations on Wing-Body-Control Configurations On Parallel Computers," AIAA Paper 96-1389, April 1996.

[10] Byun, C. and Guruswamy, G. P., "Static Aeroelasticity Computations for Flexible Wing-Body-Control Configurations," AIAA Paper 96-4059, September, 1996.

[11] Manro, M. E., Manning, K. J. R., Hallstaff, T. H. and Rogers, J. T., "Transonic Pressure Measurements and Comparison of Theory to Experiment for an Arrow-Wing Configuration," NASA CR-2610, August 1976.

[12] Guruswamy, P. and Yang, T. Y., "Aeroelastic Time-Response Analysis of Thin Airfoils by Transonic Code LTRAN2," *Computers and Fluids*, Vol. 9, No. 4, Dec. 1980, pp. 409–425.

[13] Guruswamy, P. and Goorjian, P. M., "Computations and Aeroelastic Applications of Unsteady Transonic Aerodynamics About Wings," *Journal of Aircraft*, Vol. 21, No. 1, Jan. 1984, pp. 37-43.

[14] Lee-Rausch, E. M. and Batina, J. T., "Calculation of AGARD Wing 445.6 Flutter Using Navier-Stokes Aerodynamics," AIAA-93-3476, 11th Applied Aerodynamics Conf., Monterey, CA, Aug. 1993.

[15] Chen, P. C., Sarhaddi, D. and Liu, D. D., "Transonic AIC Approach for Aeroelastic and MDO Applications," Euromech Colloquium 349, DLR, Göttingen, Germany, Sept. 16 - 18, 1996. Also to appear in May/April 1999 issue of Journal of Aircraft.

[16] Desmarais, R. N. and Bennett, R. M. "User's Guide for a Modular Flutter Analysis Software System (FAST Version 1.0)," NASA TM-78720, May 1978.

[17] Ballhaus, W. F. and Goorjian, P. M., "Computation of Unsteady Transonic Flow by Indicial Method," *AIAA Journal*, No. 2, Vol. 16, Feb. 1978, pp. 117-124.

[18] Guruswamy, G. and Tu, E., "Navier-Stokes Computations on Flexible Advanced Transport-Type Wing Configurations in Transonic Regime," AIAA Paper 94-1725, April 1994.

[19] Bland, S. R. and Edwards, J. W., "Airfoil Shape and Thickness Effects on Transonic Airloads and Flutter," AIAA-83-0959, May 1983.

[20] Byun, C. and Guruswamy, G. P., "An Efficient Procedure for Flutter Boundary Prediction on Parallel Computers," AIAA Paper 95-1484, April 1995.

[21] Message Passing Interface Forum, *MPI: A Message-Passing Interface Standard*, University of Tennessee, May 1994.

[22] Fineberg, S., "MPIRUN: A Loader for Multidisciplinary and Multizonal MPI Applications," NAS News, Vol. 2, No. 6, Nov.Dec. 1994.

[23] Byun, C. and Guruswamy, G. P., "A Comparative Study of Serial and Parallel Aeroelastic Computations of Wings," NASA TM-108805, January 1994.

[24] "ICEM-CFD User's Guide Version 3.0," Control Data Technical Publications, August 1992.

[25] Chan, W. M. and Steger, J. L., "Enhancement of a Three Dimensional Hyperbolic Grid Generation Scheme," Applied Mathematics and Computation, Vol. 51, Oct. 1992, pp. 181–205.

[26] Dogget, R. V., Rainey, A. G. and Morgan, H. G., "An Experimental Investigation of Aerodynamics Effects of Airfoil Thickness on Transonic Flutter Characteristics," NASA TM X-79, Nov. 1959.

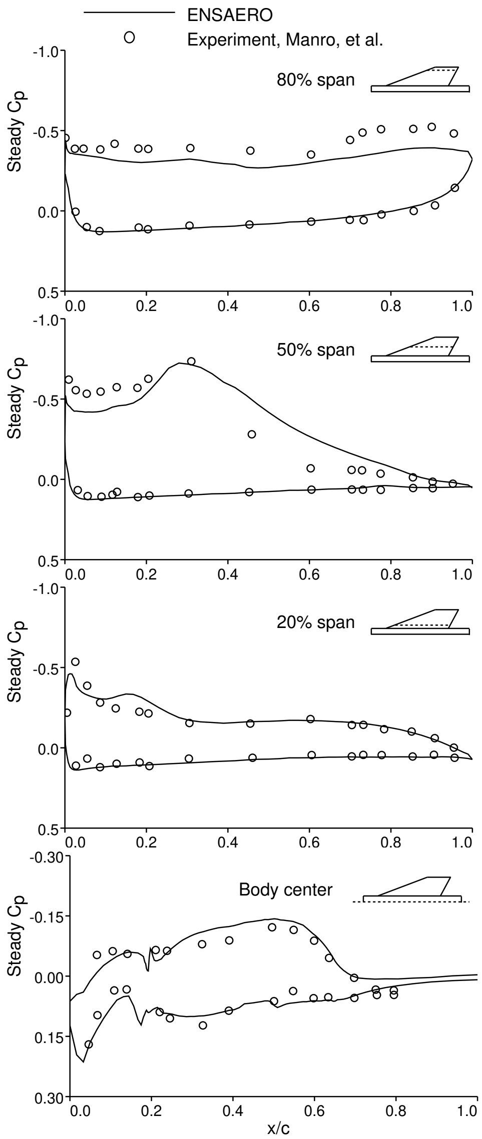

Fig. 6. Comparison of computed steady pressures with experiment; no flap deflection.

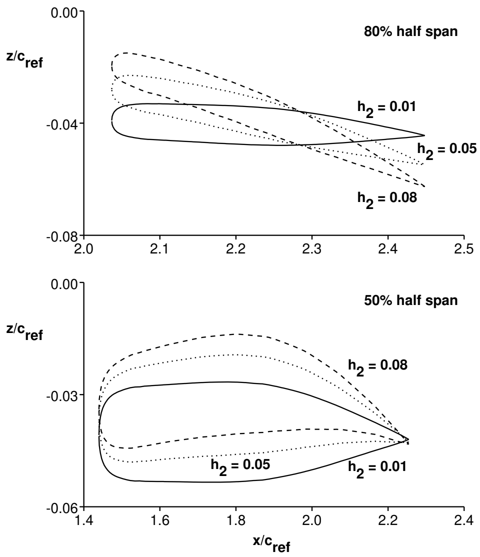

Fig. 7. Cross-sectional view of deformed wing for three different perturbation amplitudes of the second vibration mode.

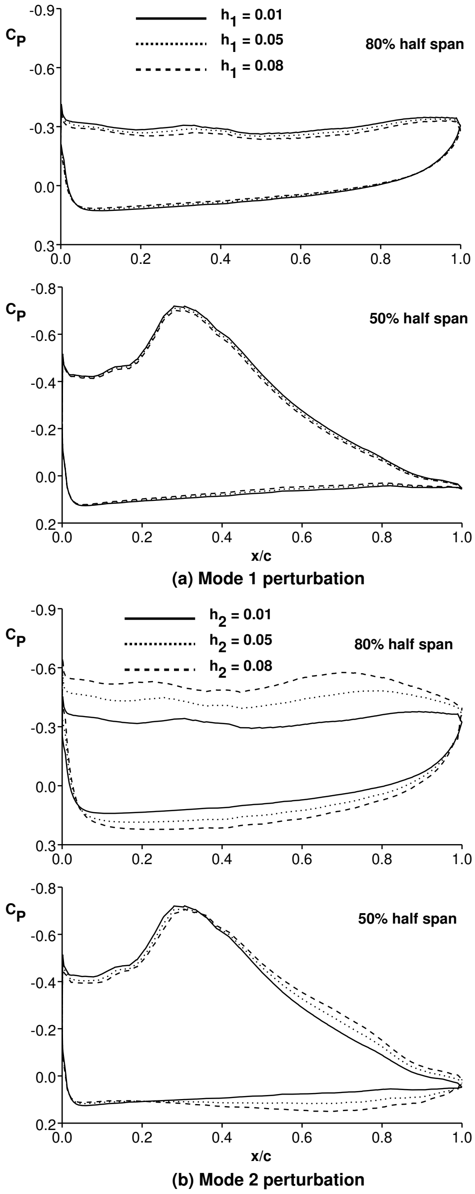

Fig. 8. Changes of sectional pressure distribution for three different perturbation amplitudes.

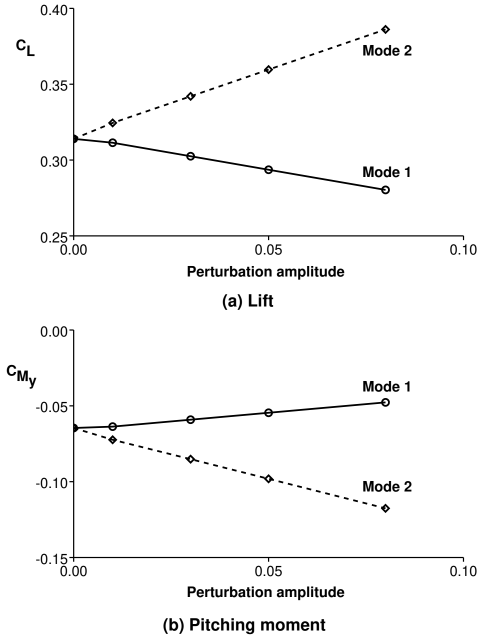

Fig. 9. Changes of lift and moment coefficients for various perturbation amplitudes.

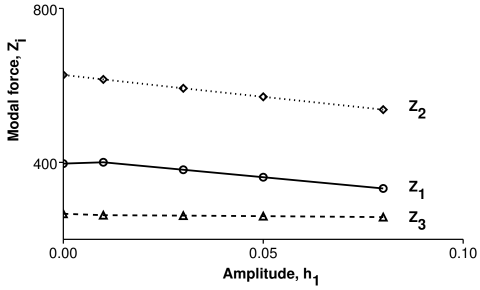

Fig. 10. Variation of modal aerodynamic forces with respect to various perturbation amplitudes of the first mode.

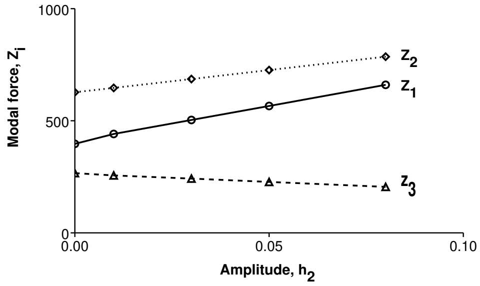

Fig. 11. Variation of modal aerodynamic forces with respect to various perturbation amplitudes of the second mode.

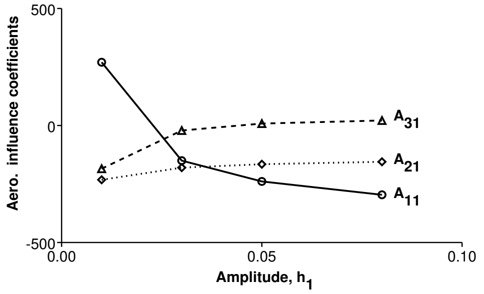

Fig. 12. Variation of aerodynamic influence coefficients due to perturbation based on the first mode.

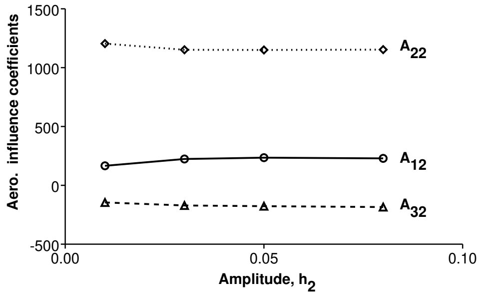

Fig. 13. Variation of aerodynamic influence coefficients due to perturbation based on the second mode.

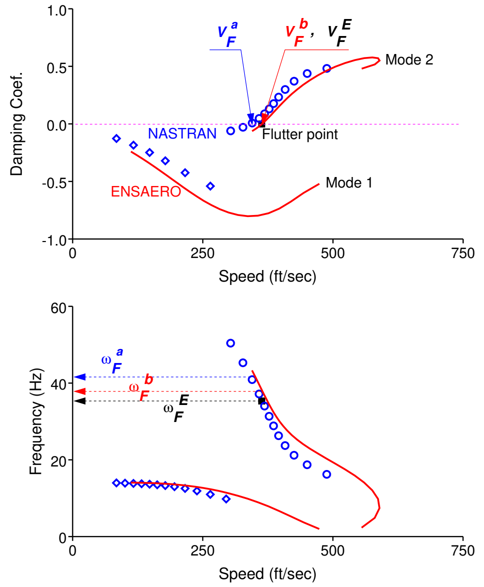

Fig. 14. Flutter speed comparison among NASTRAN, ENSAERO and the experimental results noted by superscripts a, b and E, respectively.